Modeling Earth Systems and Environment (2024) 10:651–670
https://doi.org/10.1007/s40808-023-01802-6

ORIGINAL ARTICLE

Integration of AFELA and machine learning for analysis of shallow foundation over horseshoe tunnel in rock mass

Aayush Kumar[1] · **Vinay Bhushan Chauhan**[1] · **Piyush Kumar**[1]

Received: 21 March 2023 / Accepted: 26 May 2023 / Published online: 6 June 2023

Abstract

This study investigates the stability of a uniformly distributed loaded strip footing located above a horseshoe-shaped tunnel in the rock mass. The study employs the Adaptive Finite Element Limit Analysis (*AFELA*) and machine learning approaches, including Artificial Neural Network (*ANN*) and Multiple Linear Regression (*MLR*), to assess the stability number (N_v). The study examines the impact of several governing parameters on N_v, such as the vertical (D) and horizontal (H) distance of the tunnel from the footing, Geological Strength Index (*GSI*), Uniaxial Compressive Strength (*UCS*) (σ_{ci}), and material constant (m_i) of rock mass. The study findings indicate that all parameters, except *UCS*, have a significant effect on N_v. Additionally, if the depth of the tunnel is greater than three times the width of the footing, the presence of the tunnel does not affect the stability of the footing. The dominant potential failure envelopes are evaluated based on the tunnel's position with respect to the footing, enhancing the understanding of the associated potential failure mechanisms. It also highlights the importance of governing parameters such as *H/B* and *D/B* in predicting the associated potential failure planes. The study also develops *ANN* and *MLR* models with high accuracy in predicting N_v. The sensitivity analysis provides insight into the relative significance of each input parameter affecting N_v. The findings of this study could serve as a valuable basis for establishing recommendations and design principles for the development of the infrastructure over the underground tunnels.

Keywords Adaptive finite element analysis (*AFELA*) · Artificial neural network (*ANN*) · Multiple linear regression (*MLR*) · Rock mass · Footing

Introduction

Rock mass is a highly desirable foundation material owing to its exceptional strength to withstand the applied load, making it the preferred choice for foundation construction. However, accurate determination of the ultimate bearing capacity (*UBC*) of the foundation is critical for designing engineering structures such as dams, bridges, piers, and tunnels. Furthermore, rock masses pose various challenges in construction activities such as tunnelling and pipeline laying due to micro-scale imperfections including cavities and flaws that result from long-term geological processes such as weathering and erosion (Fam et al. 2002; Waltham et al. 2005). The existence of underground structures such as tunnels, pipelines, shafts, caverns, and voids, whether natural or man-made, can pose significant safety risks for adjacent or nearby foundations. Such structures can cause settlement and reduce the ultimate bearing capacity of nearby foundations. In cases where rock masses contain tunnels or cavities, accurately determining their location in relation to the loaded area is crucial. This is because even if the tunnel or cavity is located at significant depths and horizontal distances from the foundation, it can still substantially decrease the foundation's load-carrying capacity. Previous studies have demonstrated the impact of underground structures on foundation design, making it essential to account for their interaction during design and accurately evaluate the ultimate bearing capacity of the foundation to ensure safe construction of structures above it or in the vicinity (Xiao et al. 2018, 2019; Wu et al. 2020a; Kumar and Chauhan 2022a; Kiyosumi et al. 2011;

✉ Vinay Bhushan Chauhan
chauhan.vinaybhushan@gmail.com; vbcce@mmmut.ac.in

Aayush Kumar
aayush.yadavv@gmail.com; aayush@mmmut.ac.in

Piyush Kumar
Piyushkumar199126@gmail.com

[1] Civil Engineering Department, Madan Mohan Malaviya University of Technology, Gorakhpur 273010, Uttar Pradesh, India

Ukritchon and Keawsawasvong 2018; Wang and Badie 1985; Wu et al. 2020a; Zhao et al. 2021) have examined these effects.). Previous research has extensively investigated the detrimental effects of various unlined tunnel/cavity cross-sectional shapes, such as rectangular, square, circular, or irregular, on the ultimate load-carrying capacity (*UBC*) and stability of shallow foundations. While some studies have focused on the impact of a single unlined rectangular cavity/tunnel (Kiyosumi et al. 2011; Wang and Badie 1985), many others have investigated the effects of dual cavities/tunnels on the *UBC* of shallow foundations (Xiao et al. 2019; Wu et al. 2020a).

Numerous studies in the field have shown that advanced numerical techniques can be highly effective in analyzing the interaction between cavities and footings in rock masses. For instance (Badie and Wang 1984), utilized the Finite Element Method (*FEM*) and the Upper-Bound (*UB*) theorem to initially evaluate the load-bearing capacity of footings positioned above cavities. Since then, many studies have tackled the problem of cavity/tunnel–footing interaction in rock masses by employing *FEM* under various conditions (e.g., Hoek and Brown 1980; Carranza-Torres 1998; Fraldi and Guarracino 2010).

The determination of the bearing capacity of a strip footing using Finite Element Method (*FEM*) has become subjective due to the deceptive load-settlement curve resulting from substantial displacement of the footing (Wong and Wu 2015; Lee et al. 2014; Lai et al. 2022a, b, c, d, e). To overcome the limitations of *FEM*, Finite Element Limit Analysis (*FELA*) is considered a viable method to determine the ultimate bearing capacity (*UBC*) of a foundation resting on a rock mass (Jaiswal and Chauhan 2021). *FELA* has been extensively employed for accurate determination of *UBC* of footings resting over cavities/tunnels in rock mass under various loading considerations (Chauhan et al. 2022; Kumar and Chauhan 2022a, b, c). The stability of the footing is also affected by changes in the shape, location, and rock mass parameters of the tunnel (Xiao et al. 2018, 2019; Wu et al. 2020a; Zhao et al. 2021; Kumar and Chauhan 2022a). The presence of natural structural discontinuities in rock masses such as joints, cracks, and bedding planes, particularly with significant voids, poses challenges to engineering investigations. In such cases, advanced numerical techniques, including the Generalized Hoek Brown (*GHB*) criterion (Hoek et al. 1980, 2002), a widely recognized nonlinear failure criterion for rock failures, are beneficial in understanding the issue and identifying progressive failure.

Recent advancements in shield technology have facilitated the excavation of various types of tunnels, including circular and non-circular configurations such as elliptical, rectangular, and horseshoe-shaped tunnels, in practical engineering. Among these, non-circular tunnels are preferred due to their superior section utilization and lower construction costs compared to circular tunnels. Horseshoe-shaped tunnels, in particular, are commonly used in tunnel and subway construction, especially in mountainous areas where rock excavation is necessary. These tunnels feature a semi-circular roof and two vertical wall and a horizontal bottom, offering load distribution benefits similar to those of circular tunnels, while allowing for effective section utilization. Consequently, horseshoe-shaped tunnels are considered more efficient than circular, square, and rectangular tunnels.

While several studies have investigated the effects of footings resting above single or multiple unlined tunnels of various shapes, including circular and square, no research has yet explored the impact of footings resting above a horseshoe-shaped unlined tunnel. However, limited exploration into the stability analysis of horseshoe-shaped tunnels in soil or rock mass subjected to gravity or surcharge loading is evident from the literature (Zang et al. 2018; Rehman and Kumar 2022; Liu et al. 2022; Lowongkerd et al. 2022; Jearsiripongkul et al. 2022a). Additionally, a recent study by Ahmadi et al. (2023) examined the impact of a horseshoe-shaped tunnel and metro station on adjacent deep bridge foundations in cohesive soil.

This study aims to investigate the response of a strip footing subjected to a uniformly distributed load in the presence of an unlined horseshoe-shaped tunnel within a rock mass. Accurately evaluating the ultimate bearing capacity (*UBC*) of the footing and understanding the interaction between the foundation and the underground structures are crucial for ensuring the secure construction of any nearby or on-top structures. Therefore, designers require data on the reduction in *UBC* resulting from voids or tunnels, as this information significantly impacts the project's safety and overall cost. The primary objective of this research is to provide such data to designers to ensure the secure construction of structures above or near unlined horseshoe-shaped tunnels.

Soft computing, specifically the use of artificial neural networks (*ANNs*), has emerged as a promising alternative to traditional analytical and numerical methods for solving problems. *ANNs* can generate large datasets and construct black-box predictive models using simple equations. This approach has been effective in predicting the bearing capacity of foundations in rock masses, as demonstrated by various studies. However, there are no studies available on the stability of foundations laid over a rock mass with an unlined horseshoe-shaped tunnel. To address this gap, a stability equations and stability charts were derived using Adaptive Finite Element Limit Analysis (*AFELA*), Artificial Neural Network (*ANN*), and Multiple Linear Regression Analysis (*MLR*). These equations and stability charts enable a comprehensive assessment of the stability of a footing in this particular condition, which is valuable for geotechnical engineers for safe and cost-effective design practices. The analysis considered the positional variation of the footing with respect to the horseshoe-shaped tunnel and varying critical rock parameters, including Geological Strength Index (*GSI*), material constant (m_i), uniaxial compressive strength (σ_{ci}), and disturbance factors (*DF*), all following the generalized Hoek–Brown failure criterion.

The investigation aimed to examine the influence of these parameters on the stability of a footing situated above a horseshoe-shaped tunnel. Furthermore, the potential failure mechanism of the strip footing in the presence of a horseshoe tunnel was also examined to demonstrate the effect of the positional variation of the footing with respect to tunnel and rock mass parameters on the development of failure patterns.

Problem definition

Figure 1 depicts an overview of the problem considered in the present study, which shows a weightless, rigid strip footing of width *B* resting on a rock mass with unit weight, γ. A horizontal ground overlays a rock mass containing an unlined horseshoe-shaped tunnel. The horseshoe tunnel's geometry can be described completely by two distinct segments: a flat bottom floor beneath the ceiling with a width of *W* and vertical walls with a height of *W/2*, and a semi-circular tunnel ceiling with a diameter of *W*. The relative position of the tunnel in relation to the footing is indicated by two parameters: the vertical depth, *D*, and the horizontal offset distance, *H*. *D* represent the depth of the tunnel's crest from the horizontal ground surface, and *H* represents the horizontal distance of the tunnel's crest from the footing's central vertical axis. The strip footing is subjected to a uniformly distributed load, q_u. To simplify the representation of the tunnel's dimensions and its position with respect to the footing, the distances and dimensions are normalized by the width of the footing, which is referred to as the normalized tunnel width (*W/B*), the normalized depth of the tunnel (*D/B*), and the normalized horizontal distance of the tunnel (*H/B*). Additionally, to study the positional variation of the tunnel with respect to the footing, the variation of the horizontal position of the tunnel is considered to be unidirectional, namely in the leftward direction of the footing's symmetry axis, to avail the advantage of the symmetry of the system.

In the present study, it is assumed that the rock mass follows the Generalized Hoek–Brown (*GHB*) failure criterion, which was proposed by Hoek et al. (2002) to account for the complex non-linear strength properties of rock masses. This criterion serves as a fundamental tool for accurately estimating the stability of a footing by incorporating the inherent non-linear properties of the underlying rock formations. The *GHB* failure criterion expresses a mathematical formula that enables one to determine the maximum load capacity (effective major principal stress) that a foundation can withstand before experiencing structural failure and is shown in Eq. (1).

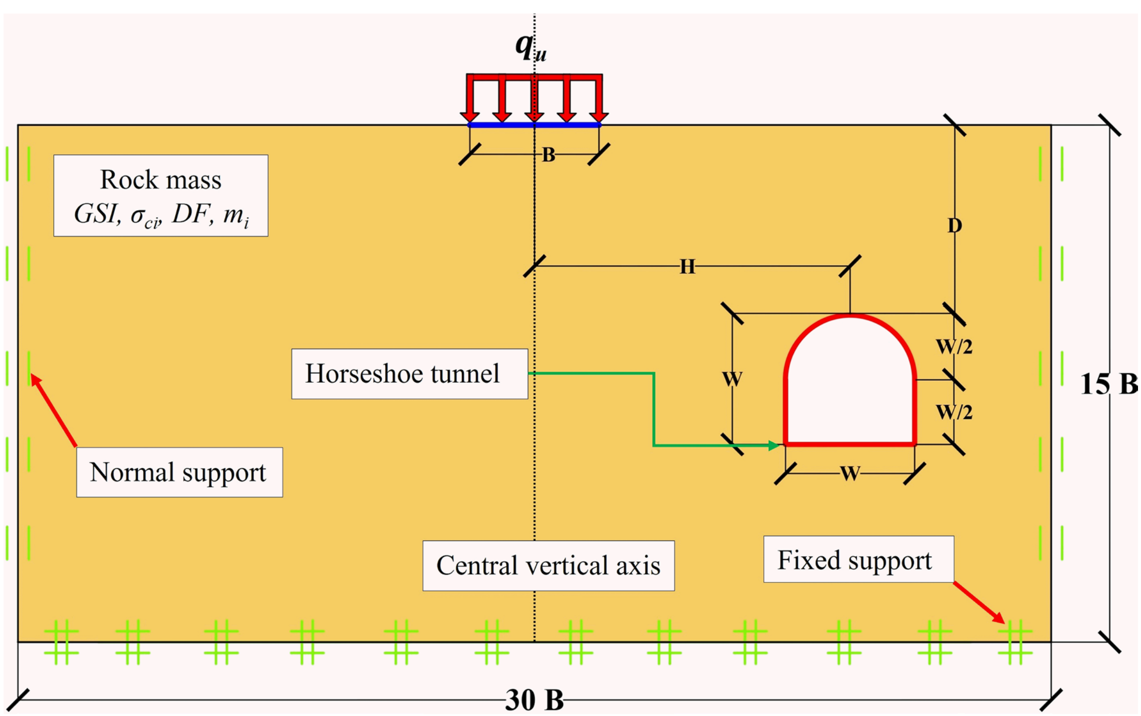

Fig. 1 Uniformly loaded strip footing supported by rock mass over a horseshoe shaped tunnel

$$\sigma_1^{'} = \sigma_3^{'} + \sigma_{ci}(m_b \frac{\sigma_3^{'}}{\sigma_{ci}} + s)^a \quad (1)$$

The variables $\sigma_1^{'}$ and $\sigma_3^{'}$, represent the effective major and minor principal stresses at point, respectively and σ_{ci} represents uniaxial compressive strength of intact rocks. The *GSI* (geological strength index) utilizes the inherent characteristics of rock types, structural arrangements, and the conditions of discontinuity substrates (Soleiman et al. 2019) present in the rock mass to determine the material parameters m_b, s, and a, via the implementation of the following empirically derived relationships shown in Eqs. (2–4).

$$m_b = m_i \exp\left(\frac{GSI - 100}{28 - 14DF}\right) \quad (2)$$

$$s = \exp\left(\frac{GSI - 100}{9 - 3DF}\right) \quad (3)$$

$$a = \frac{1}{2} + \frac{1}{6}(\exp^{\frac{-GSI}{15}} - \exp^{\frac{-20}{3}}) \quad (4)$$

The material constant for rock mass strength is denoted as m_b, whereas the constants s and a represent the Generalized Hoek–Brown failure criterion constants for the rock mass. The material constant of the intact rock, m_i is determined by the frictional properties of the minerals comprising the intact rock mass and has a significant impact on the rock's strength characteristics. The disturbance factor, *DF*, quantifies the amount of disturbance caused by blast damage, impact loading and stress relaxation on the rock mass. To evaluate the effect of an unlined horseshoe-shaped tunnel on the stability of the footing, this study proposes a stability number N_v, which is the ratio of the ultimate bearing capacity of the footing, q_u, to the unconfined compressive strength of the intact rock mass, σ_{ci}. This study further assumes that N_v is a function of various parameters as shown in Eq. (5).

$$N_v = \frac{q_u}{\sigma_{ci}} = f\left(\frac{D}{B}, \frac{H}{B}, DF, GSI, m_i, \frac{\sigma_{ci}}{\gamma B}\right) \quad (5)$$

Figure 2 presents the relevant *GHB* rock mass parameters and their corresponding values, which fall well within the recommended ranges outlined by Hoek et al. (2002). Furthermore, it portrays the intervals of *D/B* and *H/B* that were investigated in the parametric analysis.

Methodology

Adaptive Finite Element Limit Analysis (*AFELA*)

The present study developed a numerical model using finite element limit analysis with adaptive mesh refinement techniques for simulating the behavior of a strip footing in the presence of a horseshoe tunnel under uniform distributed load OPTUM G2 (Optum G2 2020) software was employed for the simulation, and to ensure accuracy, a six-noded triangular element and Gaussian integration rule were used, based on the recommendations of a previous study (Lai et al. 2022a; Kumar and Chauhan 2022a). Figure 3 shows the adaptive mesh used in the simulation comprised 8534 number of edges and 5595 triangular elements, with a finer mesh around the footing and tunnel areas where maximum changes in stress and strain occurred. The computational mesh size was set to 15*B* and 30*B* in the vertical and horizontal directions, respectively, to prevent adverse effects on the results caused by domain size and minimize the possibility of failure plane development under the footing with the mesh boundaries. The interface between the foundation material and rigid foundation was assumed to be a perfectly rough interface (Jaiswal and Chauhan 2021), and the interface factor was assigned a value of one. A sensitivity analysis was carried out by varying the total number of elements in the mesh within a range of 1500 to 19,000, and it was

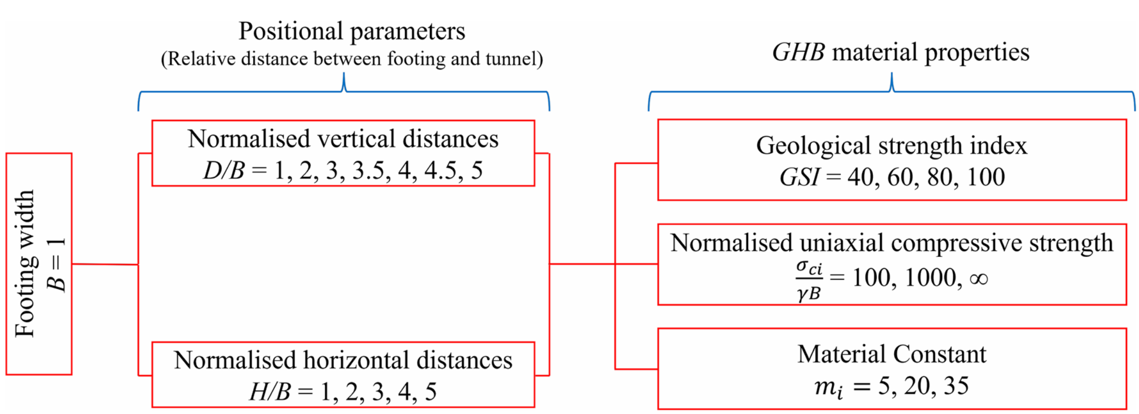

Fig. 2 Details of parameters used in the present study

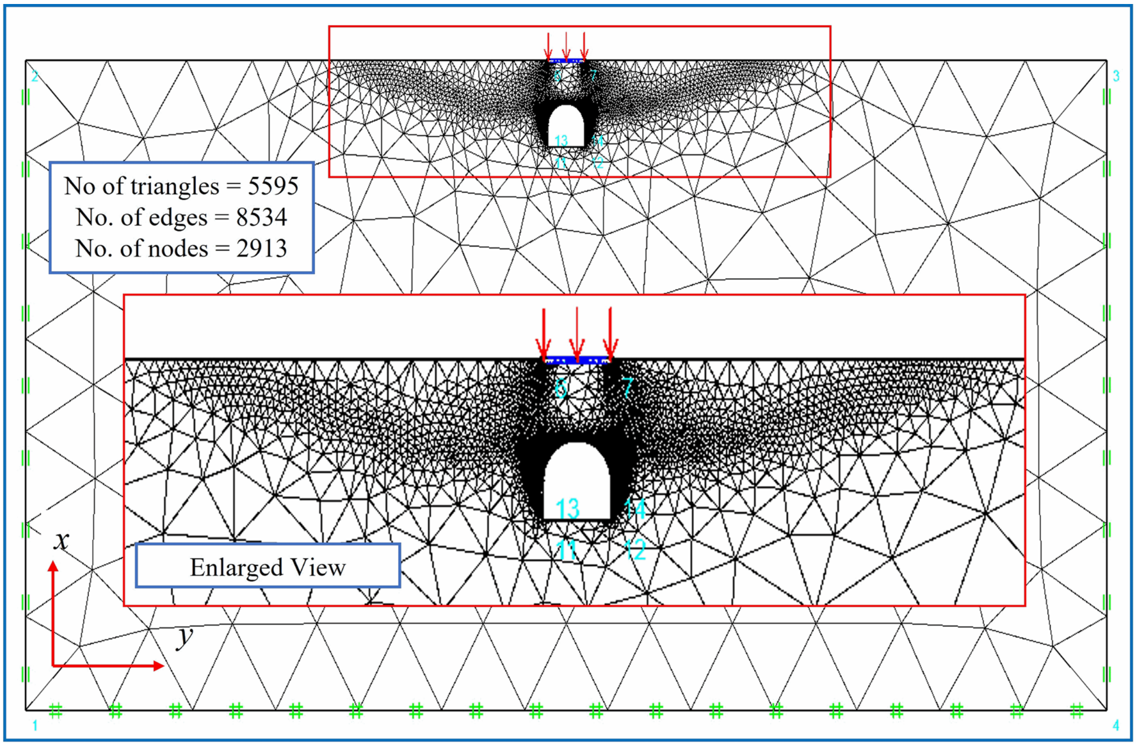

Fig. 3 Adaptive finite element mesh arrangement for the strip footing overlaying unlined horseshoe shaped tunnel in rock mass that is obtained from OPTUM G2 (2020)

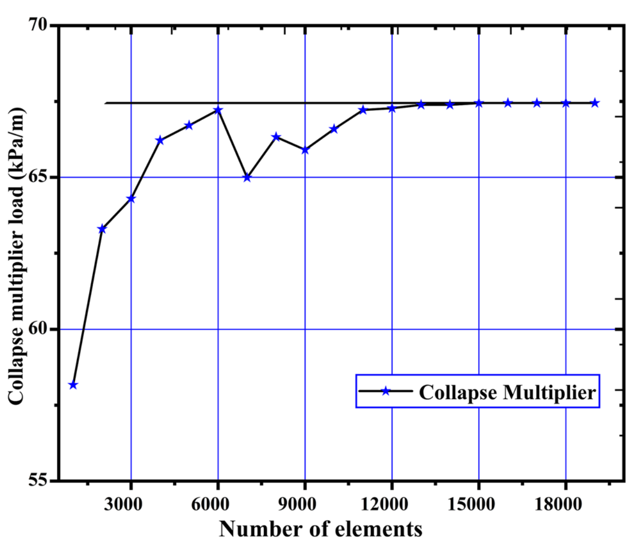

Fig. 4 Variation of collapse multiplier load with the total number of elements in the mesh

determined that 13,000 elements provided an optimal level of accuracy for the numerical model, as shown in Fig. 4.

Machine learning

Database

The study employed *AFELA* solution to generate large datasets, as shown in Fig. 2. The dataset was meticulously segregated into three distinct subsets: namely, the training, validation, and testing by 70%, 15%, and 15%, respectively. The training dataset was utilized to augment the learning process by adjusting weights. Meanwhile, the validation dataset was judiciously employed to finetune the model selection process, such as optimizing the number of hidden neurons and layers and culminating in the ultimate model determination. Finally, the testing set was employed exclusively to expound the generalizability of the trained models with remarkable proficiency.

Multiple linear regression

Linear regression is a statistical technique used for modelling the relationship between a dependent variable and one or more independent variables. The dependent variable is a single response variable, while the independent variables, also called explanatory variables, can be one or more. In the case of multiple independent variables, it is called multiple linear regression. This equation can be used to predict the value of the dependent variable based on the values of the independent variables. The equation that is used to calculate the output, which is dependent on the input or independent variables, is a linear combination of the defined variables. This is done by employing a mathematical formula, such as Eq. (6), which specifies how the independent variables should be combined to obtain the predicted value of the dependent variable.

$$y_i = \beta_0 + \beta_1 x_{i1} + \ldots + \beta_p x_{ip} + \epsilon \tag{6}$$

where y_i = dependent variable (output), $x_{i1}, x_{i2}, \ldots x_{ip}$ = independent variable (input), β_1, $\beta_2 \ldots, \beta_p$= slope coefficients, ϵ = residual error.

Artificial Neural Network (ANN)

This paper employs an Artificial Neural Network (*ANN*) to provide a data interpretation platform based on the inherent characteristics of the human brain's composition. Several studies (Azarafza et al. 2021; Jearsiripongkul et al. 2022a; Lai et al. 2022a, c, d; Sirimontree et al. 2022; Jearsiripongkul et al. 2022b; Ngamkhanong et al. 2022; Yodsomjai et al. 2022) demonstrate that the use of Artificial Neural Networks (*ANNs*) is a highly effective soft-computing approach in civil engineering. *ANNs* are machine learning algorithms that can recognize patterns and make predictions based on input data (Ansari et al. 2023). The neural network is composed of many interconnected nodes, or neurons, which create a computer model. The *ANN* model is made up of three layers: the output layer, the hidden layer, and the input layer. The input layer transmits the feature vector. During the learning process, the network's weights are incrementally modified

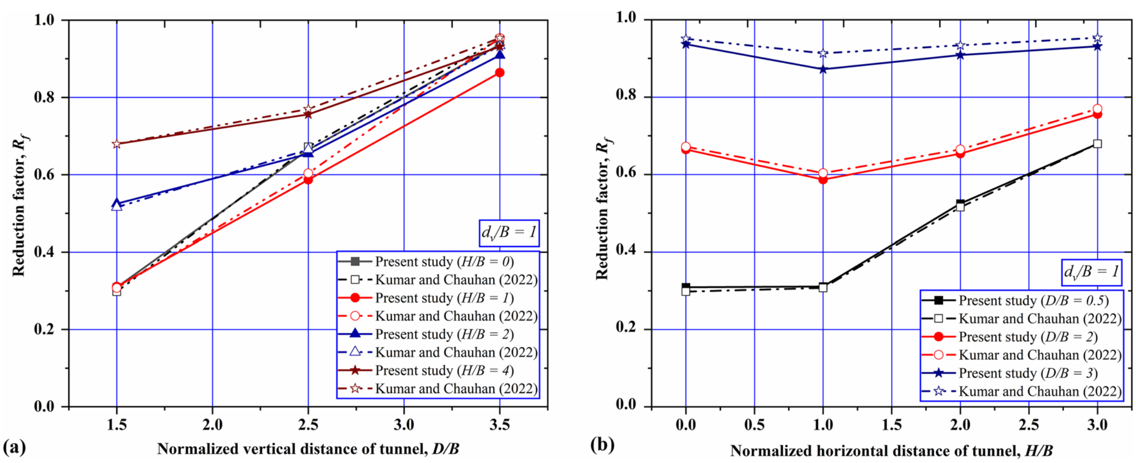

Fig. 5 Comparison of reduction factor, R_f obtained from present study and former study (Kumar and Chauhan 2022) for different values of **a** D/B; and **b** H/B

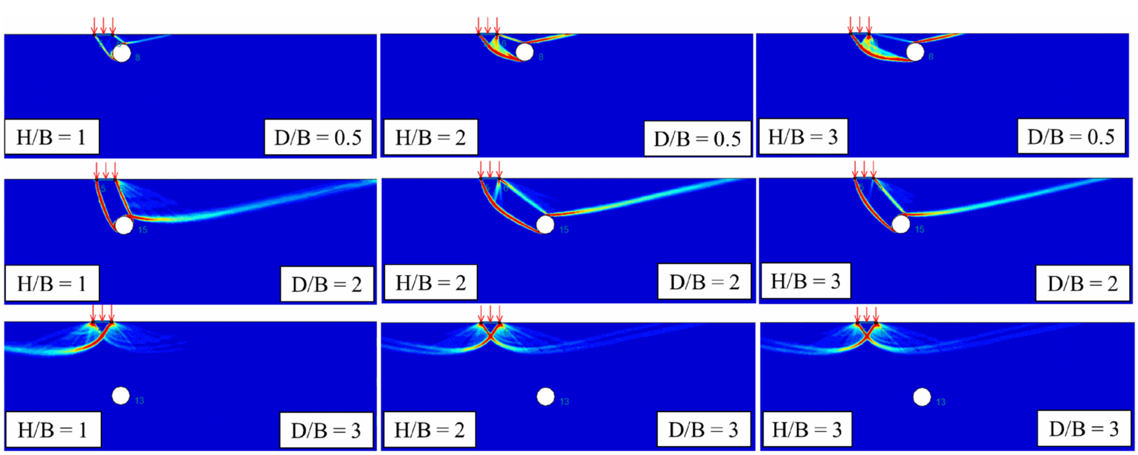

Fig. 6 Potential failure envelopes of strip footing resting above circular tunnel for various position-validation study

until they achieve an appropriate level of accuracy to predict the target with reasonable precision. This technique is particularly effective in addressing nonlinear problems, as stated by Park and Lek (2016).

This investigation uses an input layer comprising of four sets of five input nodes each, which correspond, respectively, to the parameters *D/B*, *H/B*, *GSI*, m_i, and $\sigma_{ci}/\gamma B$. The second layer is known as the hidden layer, which consists of one or multiple threshold logic unit layers. The optimal configuration of hidden layers and neurons is usually obtained through trial and error, starting with a single hidden layer, followed by varying the number of hidden neurons from one to the maximum value that yields an accurate model. The primary function of the hidden layer is to process the input information and transform it into a format that can be efficiently used by the output layer to generate predictions. The hidden layer computes weighted sums of inputs and applies a step function to them using the rectified linear unit (*ReLU*) activation function, which adds nonlinearity to the network. The output layer presents dependent variables, and in this paper, it consists of a single node that predicts the N_v.

Additionally, *LM* back-propagation algorithm is utilized to determine output parameters, achieving second-order training speeds without the need to compute the Hessian matrix. The *LM* algorithm modifies weight and bias values and provides the advantages of both the Gauss–Newton technique and gradient descent algorithm, addressing the limitations of other algorithms. The *LM* algorithm is an improved Newton approach, as demonstrated by Eq. (7).

$$x_{k+1} = x_k - [J^T J + uI]^{-1} J^T e \tag{7}$$

where x_k = weight, J = Jacobian matrix, I = identity matrix, e = vector, k and u = damping factor. By adjusting damping, the accuracy and performance of the supervised algorithm can be improved based on stage outcome. Although this may require additional storage, it is recommended as the first-choice algorithm. The effectiveness of the *ANN* model is evaluated in this study using two statistical indicators:

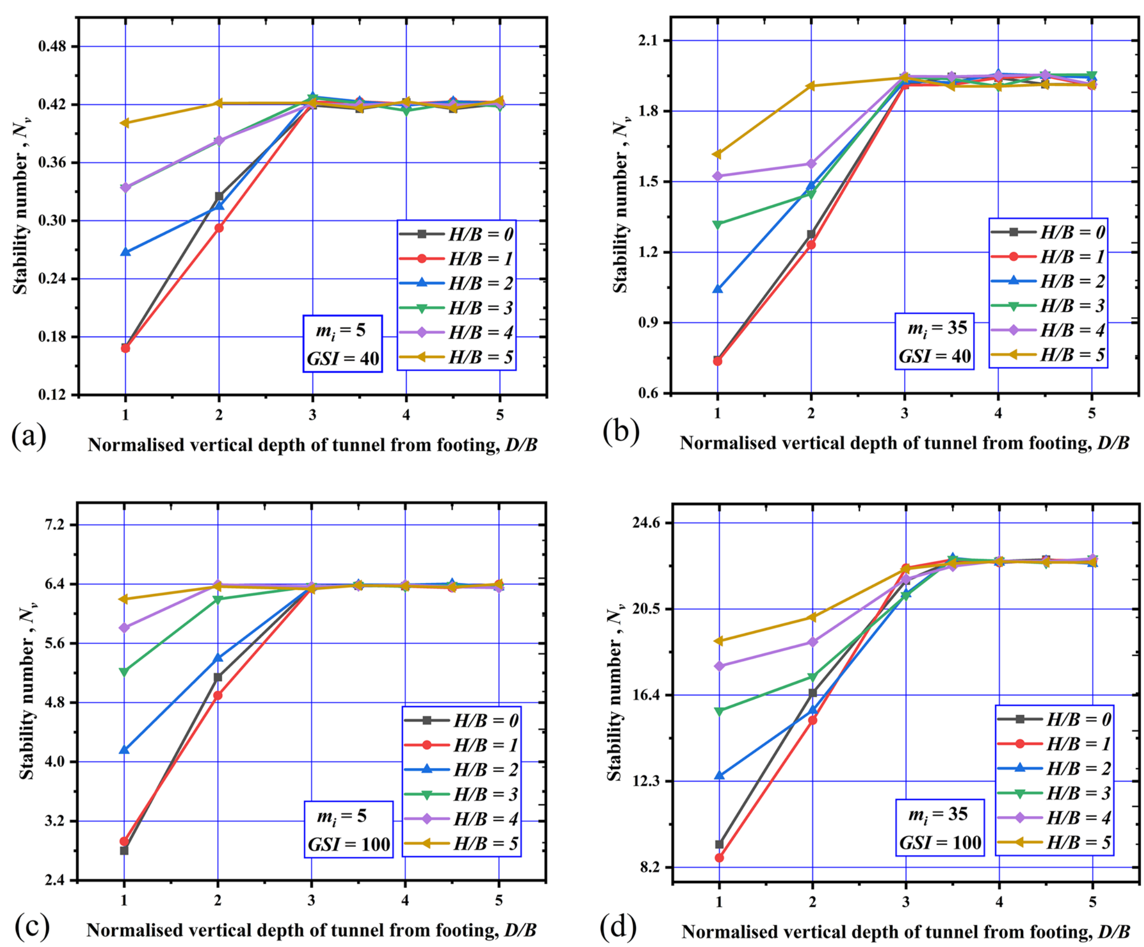

Fig. 7 Effect of *D/B* on N_v for varying *H/B* for **a** low *GSI*, low m_i (GSI = 40, m_i = 5); **b** low *GSI*, high m_i (GSI = 40, m_i = 35); **c** high *GSI*, low m_i (GSI = 100, m_i = 5); and **d** high *GSI*, high m_i (GSI = 100, m_i = 35)

Mean Squared Error (*MSE*) and the coefficient of determination (R^2). The *MSE* is the average value of a function used to construct a regression model that minimizes the sum of squared errors (*SSE*), which measures the difference between predicted and actual values. Atici (2011) describes the calculation of *MSE* and *RMSE* in Eqs. (8) and (9). Furthermore, Mean Squared Error (*MSE*) is commonly used, but Root Mean Squared Error (*RMSE)* is occasionally preferred as it provides a similar error scale to the predicted value. *MSE* is easy to alter mathematically and frequently used in mathematical approaches. *RMSE* is used more often than *MSE* to compare regression model performance against random models. Lower *MSE* and *RMSE* values indicate higher model accuracy. where 'n' and $(y_i^{'} - y_i)$ represent the number of samples and the difference between predicted and actual values on testing datasets, respectively.

$$MSE = \frac{1}{n}\sum_{i=1}^{n}(y_i^{'} - y_i)^2 \tag{8}$$

$$RMSE = \sqrt{\frac{1}{n}\sum_{i=1}^{n}(y_i^{'} - y_i)^2} \tag{9}$$

In this study, the effectiveness of trained models is assessed by utilizing the coefficient of determination (R^2), as defined in Eq. (10).

$$R^2 = 1 - \frac{\sum_{i=1}^{n}(y_i^{'} - y_i)^2}{\sum_{i=1}^{n}(y_i - \overline{y})^2} \tag{10}$$

R^2 is a measure of the proportion of real-value fluctuations that can be explained by changes in the predicted value, with a range of values between 0 and 1. The numerator and denominator of the equation mentioned above represent the difference between actual and predicted values on testing datasets and the sum of squared differences between true values and the mean, respectively (Bilim et al. 2008). A higher R^2 value indicates a better fitting effect, implying that the model can explain a larger proportion of the variability in the data.

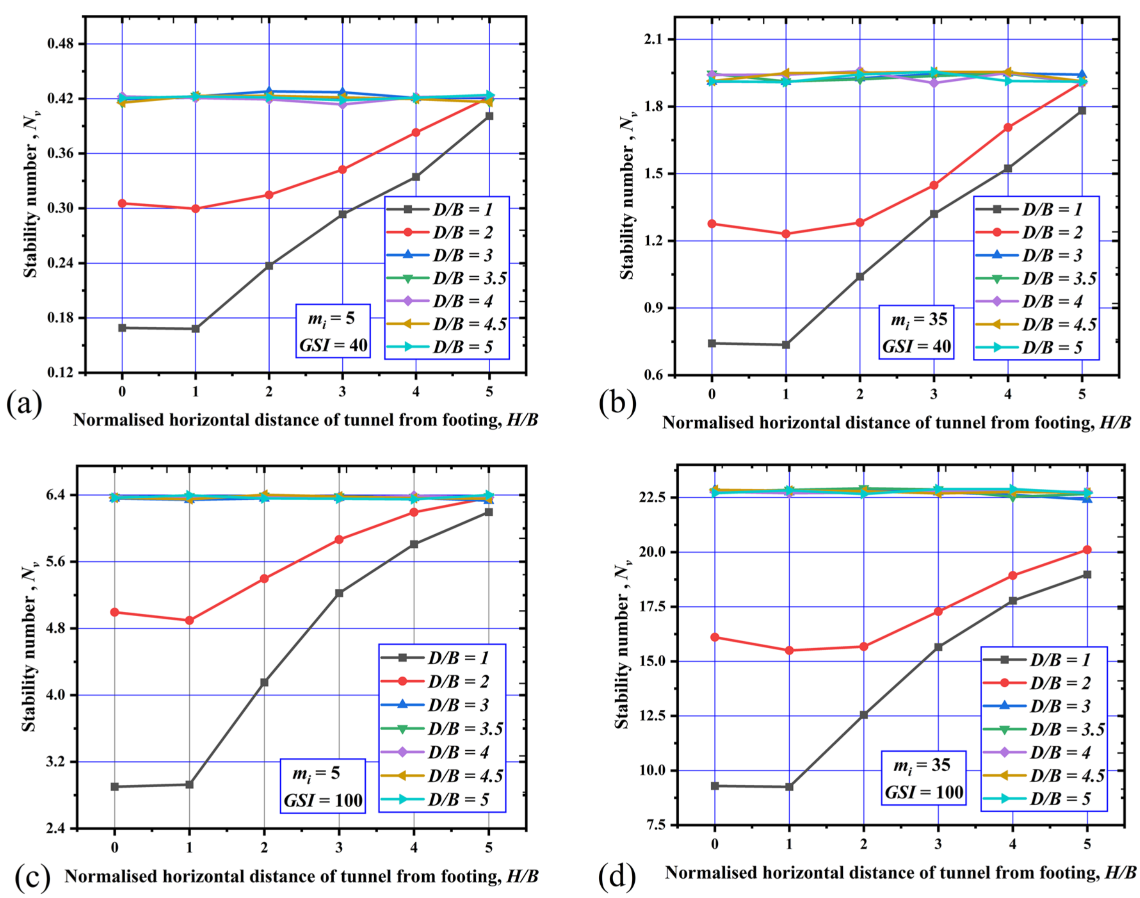

Fig. 8 Effect of *H/B* on N_v for varying *D/B* for **a** low *GSI*, low m_i (*GSI* = 40, m_i = 5); **b** low *GSI*, high m_i (*GSI* = 40, m_i = 35); **c** high *GSI*, low m_i (*GSI* = 100, m_i = 5); and **d** high *GSI*, high m_i (*GSI* = 100, m_i = 35)

Validation of *AFELA* model

In this study, the accuracy and effectiveness of a numerical model based on *AFELA* is evaluated by comparing it to the results of a former study conducted by Kumar and Chauhan (2022a). The behavior of a strip footing on an unlined circular tunnel in rock mass is analyzed using the proposed model and compared to the results of the previous study. The ultimate bearing capacity (*UBC*) values obtained from finite element limit analysis with a six-noded Gaussian element are compared and presented in Fig. 5, with the reduction factor (R_f) used to quantify the effect of the tunnel on the *UBC*. The results show (Fig. 5a) that the trends in the variation of the simulated model are similar to those reported in the previous study, with a difference in the magnitude of R_f of approximately 4% at $H/B = 1$ and $D/B = 3.5$.

Similarly, Fig. 5b shows that the trends in the variation of R_f in this model are slightly lower than those reported in the previous study, with a maximum deviation in the magnitude of R_f of less than 3.3%. Additionally, potential failure envelopes for the strip footing with the tunnel/void located at various positions are compared in Fig. 6, and the results obtained from the numerical model used for validation are similar to those of the previous study. Based on the comparison of the findings and discussion, it can be concluded that the proposed model is suitable for conducting further investigations.

Results and discussion

This section presents the results related to the impact of geometrical parameters, such as the normalized horizontal distance (*H/B*) and normalized depth (*D/B*) of a horse-shoe shaped unlined tunnel relative to the centre of a footing, as well as the influence of rock mass strength parameters, such as the geological strength index (*GSI*), the material constant of rock mass (m_i), and the normalized uniaxial compressive strength ($\sigma_{ci}/\gamma B$), on the stability of the footing as measured by stability number, N_γ. The analysis also presents the impact of various governing parameters on the potential

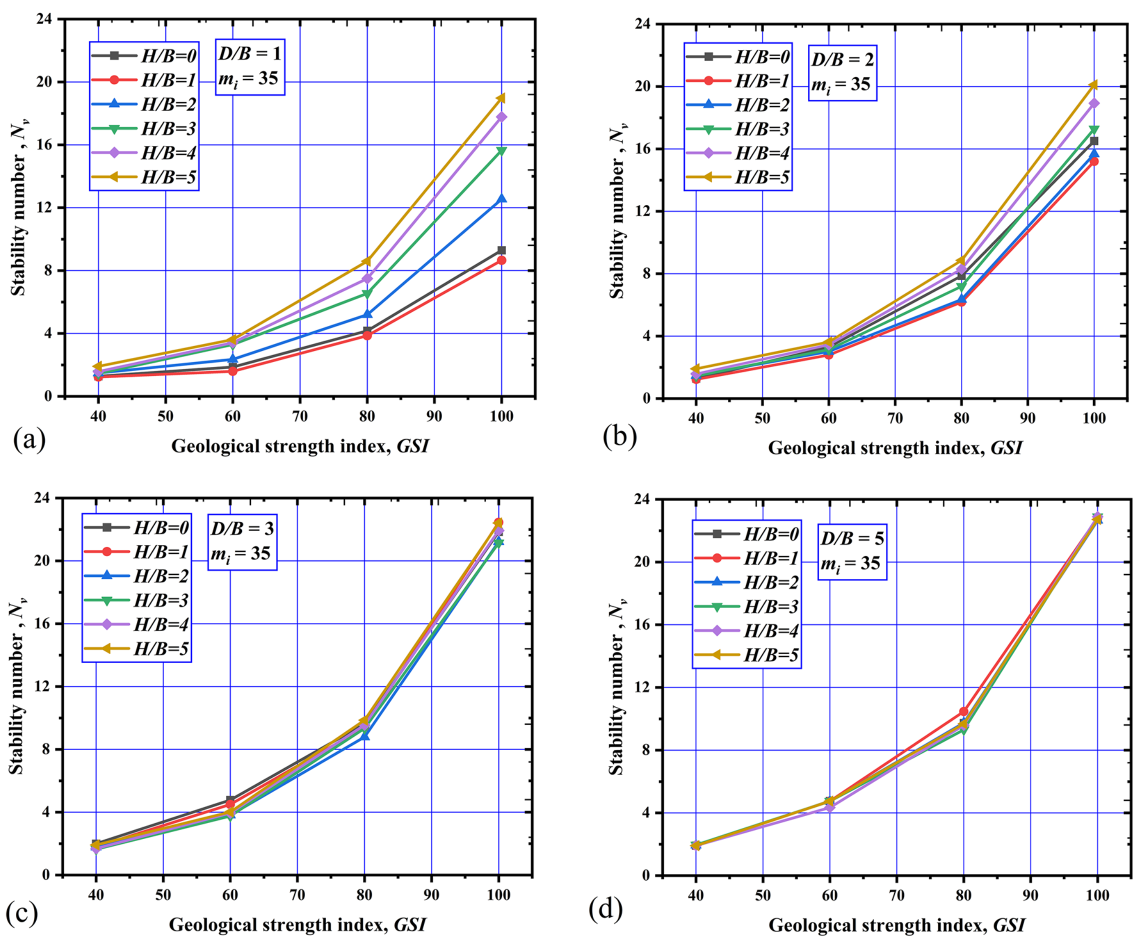

Fig. 9 Effect of *GSI* on N_γ for high m_i ($m_i = 35$) with varying *H/B* for **a** $D/B = 1$; **b** $D/B = 2$; **c** $D/B = 3$; and **d** $D/B = 5$

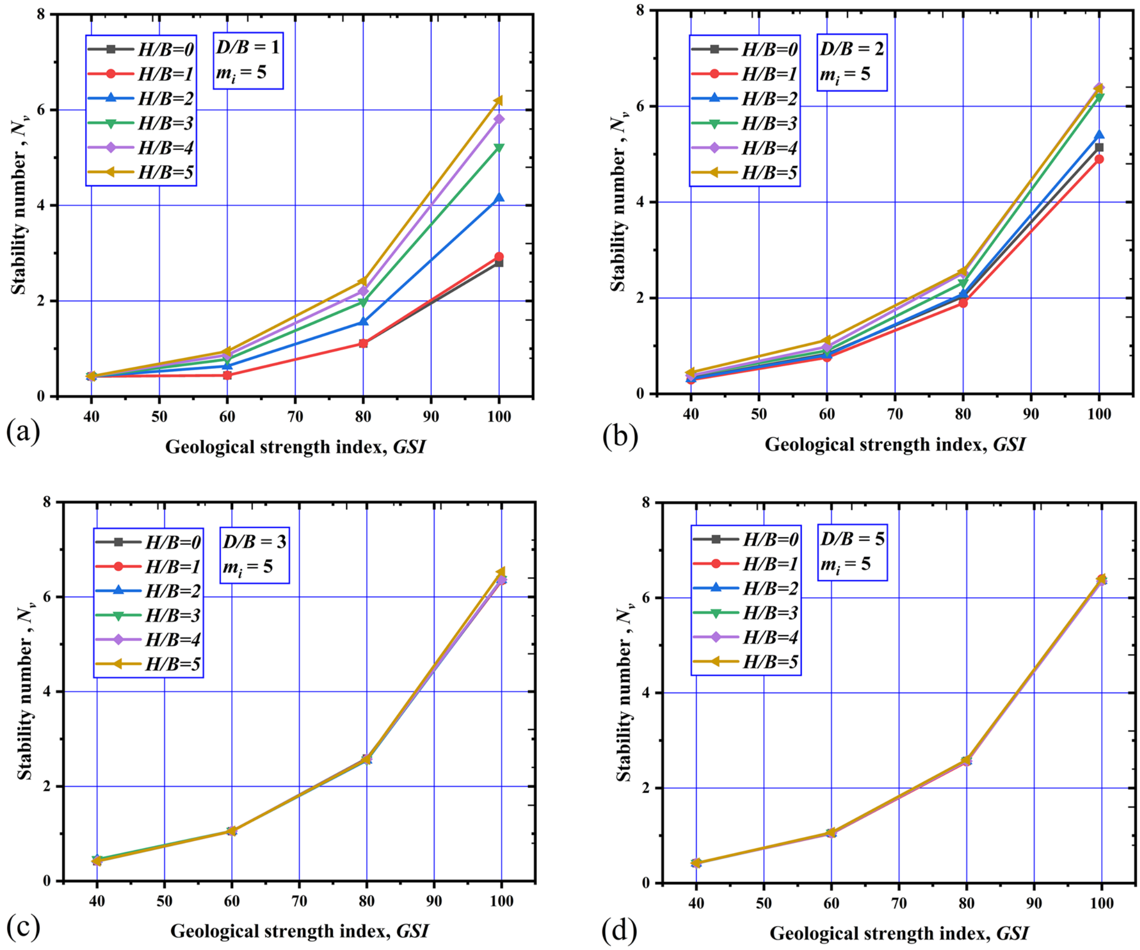

Fig. 10 Effect of *GSI* on N_v for low m_i ($m_i=5$) with varying *H/B* for **a** $D/B=1$; **b** $D/B=2$; **c** $D/B=3$; and **d** $D/B=5$

failure envelope of a strip footing caused by the presence of a tunnel in the rock mass.

Effect of *D/B* on N_v for different *H/B*

The effect of *D/B* on the bearing capacity factor (N_v) for various *H/B* is presented in four distinct scenarios, namely, low *GSI*-low m_i, low *GSI*-high m_i, high *GSI*-low m_i, and high *GSI*-high m_i, in Fig. 7a–d, respectively. The results indicate that N_v increases rapidly with an increase in the offset distance of the tunnel from the footing for depth ratios less than 3. This can be attributed to the fact that as the depth of the tunnel from the footing increases, the impact of the tunnel on the footing's ultimate bearing capacity decreases rapidly, thereby increasing N_v. However, beyond a specific threshold depth of tunnel, i.e., $D/B \geq 3$, the N_v becomes almost constant, and all values of N_v coincide irrespective of horizontal offset distance. This threshold depth is referred to as the critical depth. Beyond this depth, the effect of the tunnel on the footing's bearing capacity is negligible, and the scenario is similar to that of a footing resting on rock mass without any tunnel.

The pattern of all curves in Fig. 7a–d is almost identical for any given values of m_i and *GSI*. However, it is observed that the magnitude of N_v increases with an increase in m_i, irrespective of the *GSI* values. This trend is supported by a comparison of Fig. 7a–d, which reveal that the percentage increases in the magnitude of N_v for $m_i=35$ is approximately 3.6 times and 2.5 times greater than that for $m_i=5$, for *GSI* values of 40 and 100, respectively.

This suggests that the stability of a footing is more significantly influenced by m_i for rock masses with lower *GSI* values compared to those with higher *GSI* values. Hence, the effect of m_i on the stability of the footing is more prominent when the rock mass exhibits lower strength characteristics, as indicated by lower *GSI* values.

Moreover, a comparing Fig. 7a–d reveals that the maximum difference in the magnitude of N_v, between minimum and maximum values of *H/B* (i.e., $H/B=0$ to 5) for $D/B=1$, 2, and 3, is approximately 2.25 times, 1.4 times, and 1.01 times, respectively. This indicates that the change in N_v is

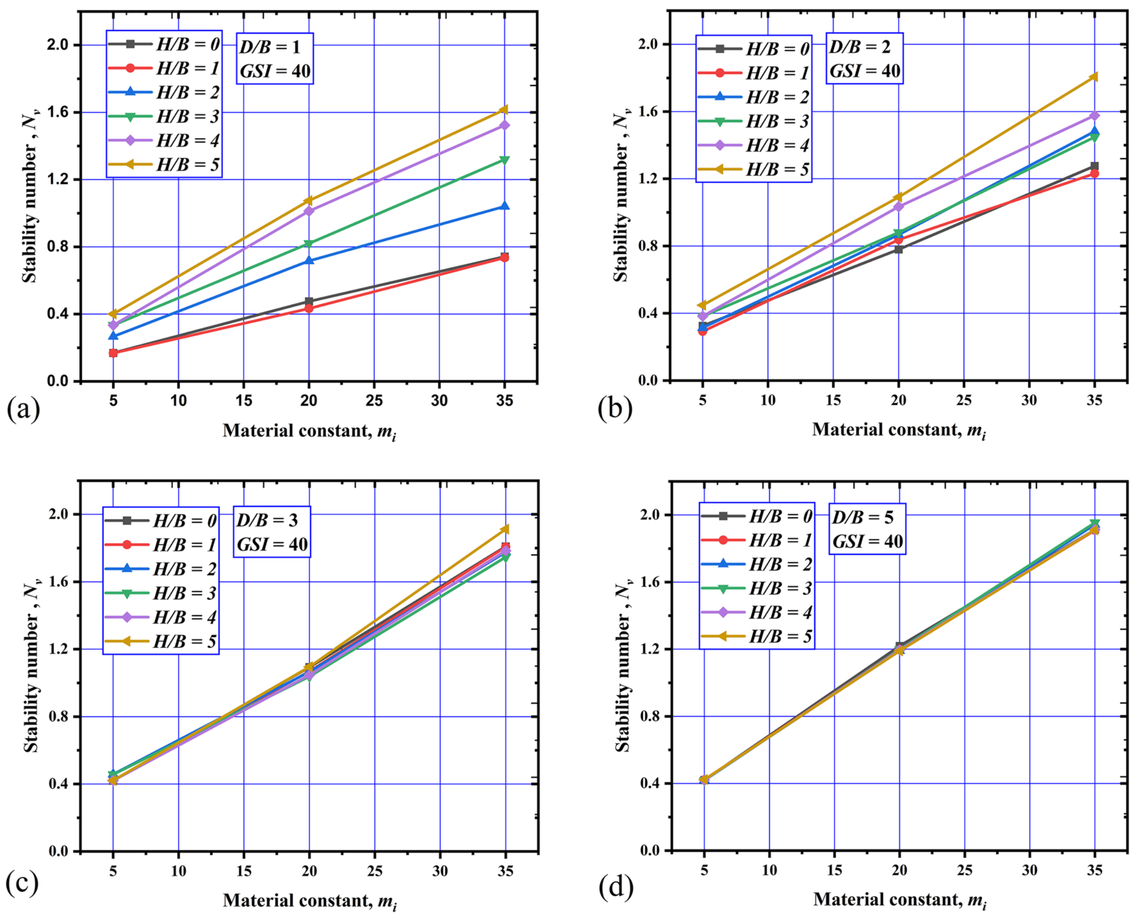

Fig. 11 Effect of m_i on N_v for low *GSI* (*GSI* = 40) with varying *H/B* for **a** *D/B* = 1; **b** *D/B* = 2; **c** *D/B* = 3; and **d** *D/B* = 5

not solely dependent on *H/B* and *D/B* because the percentage difference in N_v remains constant for a given tunnel depth among all the cases presented in Fig. 7. However, the change in the magnitude of N_v is influenced by varying the rock parameters such as *GSI* and m_i.

Effect of *H/B* on N_v for different *D/B*

Figure 8a–d illustrate the effect of the tunnel's horizontal offset distance from the footing, *H/B*, on N_v for different values of *D/B* and rock mass properties (Low *GSI*-Low m_i, Low *GSI*-High m_i, High *GSI*-Low m_i, and High *GSI*-High m_i, respectively). The analysis reveals that N_v increases with an increase in *H/B*, and this effect is more prominent at smaller values of *D/B*. However, for *D/B* ≥ 3, the effect of *H/B* on N_v becomes negligible, and the trend lines for all *H/B* values merge with each other.

Furthermore, a comparison between the curves for *H/B* = 0 and 1 shows a similar trend for N_v, except for *D/B* = 2, where N_v for *H/B* = 1 is marginally lower than N_v for *H/B* = 0. This deviation might be due to the non-uniform loading on the tunnel caused by the unsymmetrical position of the tunnel at *H/B* = 1, leading to a lower load-bearing capacity of the footing compared to the case of symmetrical loading at *H/B* = 0.

Effect of *GSI* on N_v for different *H/B*

Figures 9 and 10 display the plots of N_v versus *GSI* for two different values of m_i (i.e., 5 and 35) and varying *H/B* (0–5) while maintaining $\sigma_{ci}/\gamma B = 100$ constant for *D/B* (1, 2, 3, and 5). The plots demonstrate a nonlinear relationship between N_v and *GSI*, with N_v increasing for all values of *H/B*, *D/B*, and m_i. The increase in N_v with *GSI* is more significant for higher values of *H/B*, especially for a tunnel located at a shallow depth from the horizontal ground (i.e., *D/B* = 1 and 2). However, for tunnels situated at *D/B* ≥ 3, N_v does not vary with change in *H/B* for any given value of *GSI*. As the tunnel depth increases, the impact of *H/B* diminishes in relation to higher *GSI*. This observation is explained by the fact that the stability of the footing is primarily controlled by *GSI* when the tunnel is situated far enough vertically and horizontally from the centre of the footing. Higher *GSI* values represent a stronger and

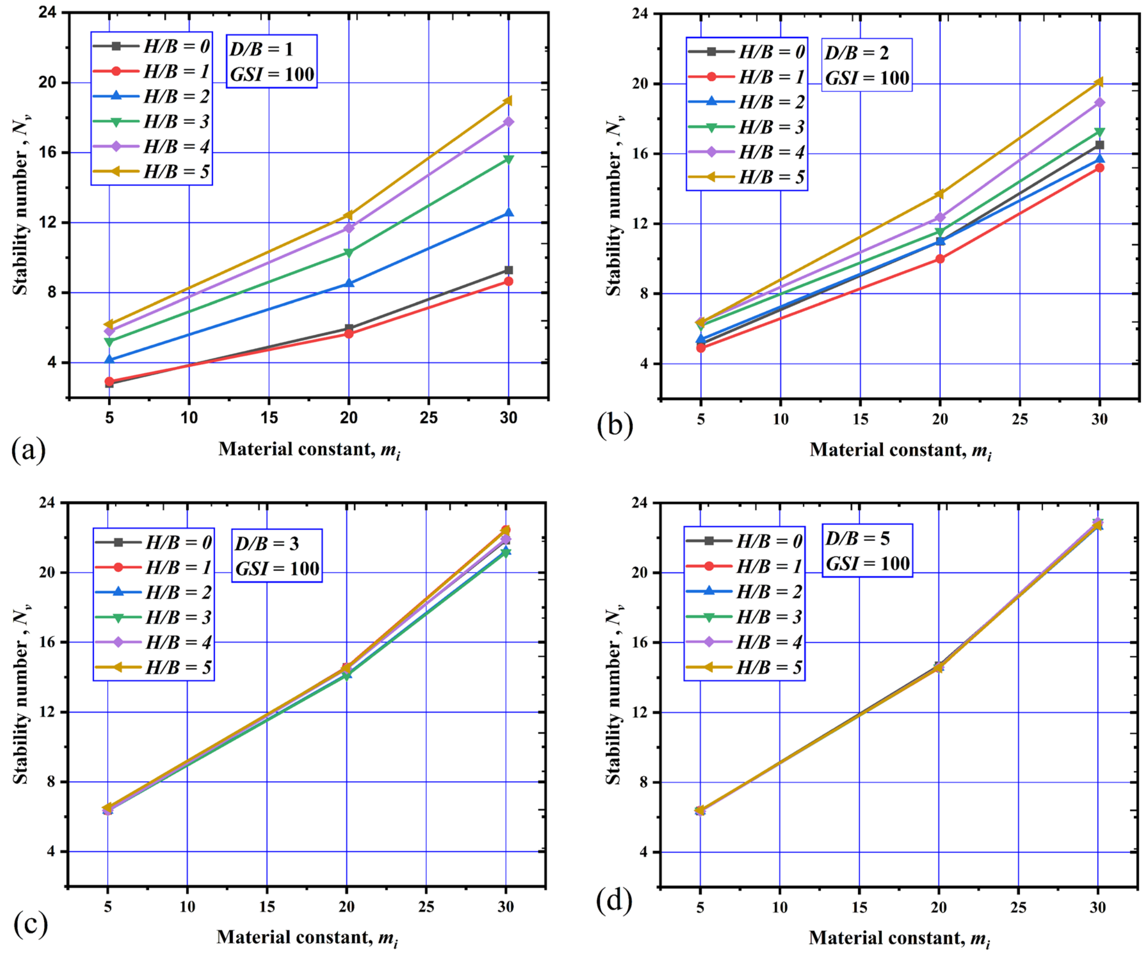

Fig. 12 Effect of m_i on N_γ for high *GSI* (*GSI* = 100) with varying *H/B* for **a** *D/B* = 1; **b** *D/B* = 2; **c** *D/B* = 3; and **d** *D/B* = 5

less fractured rock mass, resulting in an increase in the magnitude of N_γ and improved stability of the footing. The effect of *GSI* is more pronounced for larger values of *H/B*, with changes in N_γ ranging from 3.5 to 8.5 times as *GSI* increases from 40 to 100 for *D/B* = 1.

Figures 9 and 10 also compare the impact of *GSI* on N_γ for extreme values of m_i (i.e., 5 and 35). It is noted that as m_i decreases, the magnitude of N_γ also decreases. For low m_i values, the curves of N_γ versus *GSI* are identical for all ranges of *H/B* beyond *D/B* ≥ 3, indicating that *GSI* has no effect on N_γ for a tunnel in a rock mass with low m_i. However, for high m_i values, a marginal variation of N_γ versus *GSI* is noted for various values of *H/B*, even at *D/B* ≥ 3.

Effect of m_i on N_γ for different *H/B* and *D/B*

Figures 11 and 12 depict the effect of the parameter m_i on N_γ for two distinct values of *GSI*, 40 and 100, respectively. An increasing linear correlation is observed between m_i and N_γ, throughout the range of *H/B* corresponding to *D/B*. This phenomenon can be attributed to the diverse factors that influence m_i, such as mineralogy, composition, degree of interlocking, and grain size of the intact rock. As m_i increases, the rock mass's governing parameters, including grain packing patterns, interlocking degree between rock particles, and angularity, also increase. These factors contribute to an increased rock strength, leading to a higher value of N_γ. In addition, for low values of m_i, the N_γ—*GSI* curves are similar for all *H/B* ranges beyond *D/B* ≥ 3, indicating that the rock mass has low m_i. Moreover, the stability of a footing resting over a tunnel is not affected by the variation of *H/B* when the tunnel is located at *D/B* ≥ 3, given a particular m_i and *GSI* value.

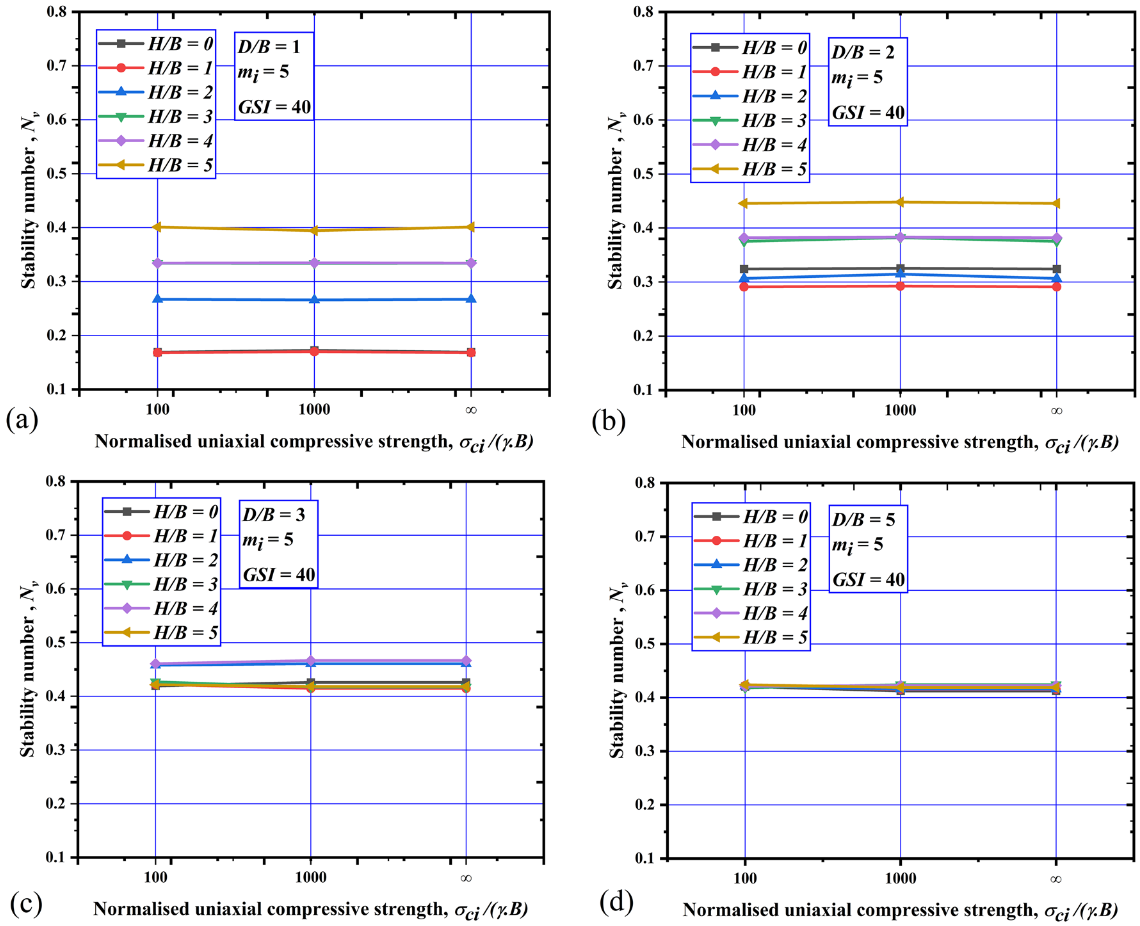

Fig. 13 Effect of $\sigma_{ci}/\gamma B$ on N_v for low *GSI* ($GSI=40$) and low m_i ($m_i=5$) with varying *H/B* for **a** $D/B=1$; **b** $D/B=2$; **c** $D/B=3$; and **d** $D/B=5$

Effect of $\sigma_{ci}/\gamma B$ on N_v for different *H/B* and *D/B*

Figures 13 and 14 illustrate plots of $\sigma_{ci}/\gamma B$ versus N_v for two different *GSI* values of 40 and 100, respectively, while m_i is kept constant at 35. It is observed that the trend of N_v for a given *H/B* and *D/B* remains unchanged, regardless of the variation in $\sigma_{ci}/\gamma B$. This results in all the curves being parallel to the x-axis. It is noted that the authors assumed $\sigma_{ci}/\gamma B=\infty$, which is not physically possible for rocks in a weightless state (i.e., $\gamma=0$) (Keawsawasvong and Shiau 2022). However, the outcomes obtained by assuming $\sigma_{ci}/\gamma B=\infty$ indicate that the rock is very strong. In numerical simulations, $\sigma_{ci}/\gamma B=\infty$ can be achieved by assigning a very large value of *UCS* or a very light rock mass to produce valid numerical results. It is interesting to note that the observed trends are independent of the *GSI* value, as demonstrated in the cases of low (Fig. 13) and high (Fig. 14) *GSI* values of the rock mass.

Multiple linear regression

In this study, the *WEKA* software is used to create a multiple regression model to examine the relationship between predictor variables and a response variable. The fitted regression weights or coefficients to the model using sophisticated algorithms that minimized the difference between the predicted and actual values of the response variable. These coefficients represent the influence of each predictor variable on the response variable. As a result of this optimization process, authors derived Eq. (11) for multiple linear regression, which expresses the complex relationship between the predictor variables and the response variable in mathematical terms.

$$
\begin{aligned}
N_v = {} & (0.187\sigma_{ci}/(\gamma B)) + (12.249GSI) + (2.148D/B) \\
& + (0.6208H/B) + (6.2637m_i) - 5.0749
\end{aligned}
\tag{11}
$$

Figure 15 compares stability factor assessed by *FELA* with predicted values obtained from *MLR*. Statistical tests such as coefficient of determination (R^2) and Root Mean

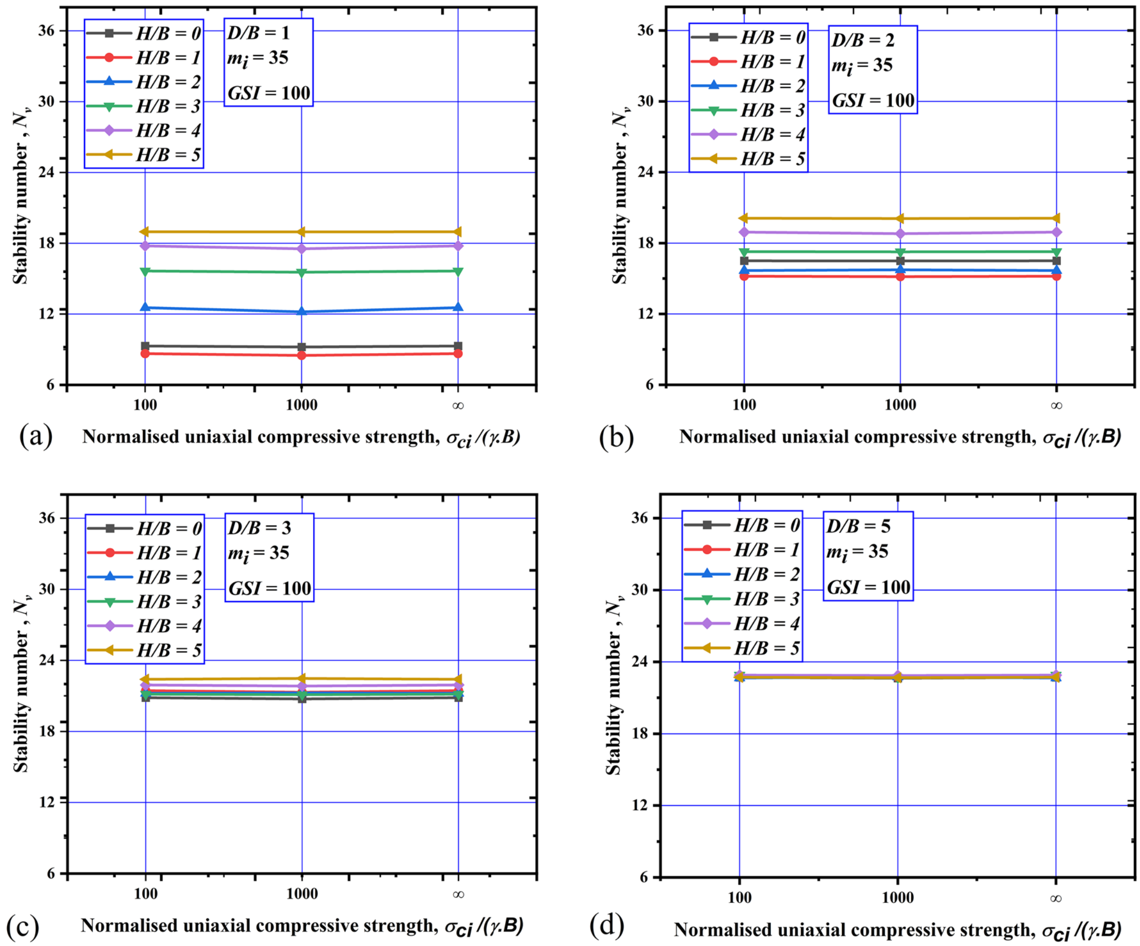

Fig. 14 Effect of $\sigma_{ci}/\gamma B$ on N_v for high *GSI* (*GSI* = 100) and high m_i (m_i = 35) with varying *H/B* for **a** *D/B* = 1; **b** *D/B* = 2; **c** *D/B* = 3; and **d** *D/B* = 5

Square Error (*RMSE*), which yield corresponding values of 0.86 and 3.1247, respectively, can be used to evaluate the effectiveness of the Eq. (10). Whereas the sensitivity analysis results are presented in Fig. 16, highlighting the relative importance of five dimensionless parameters. The Relative Importance Index (*RII*) is used to quantify the significance of each parameter, with a value of 100% denoting the highest importance. The Geological Strength Index (*GSI*) is identified as the most critical parameter with an *RII* value of 100%. The other parameters, including (m_i), (*D/B*), (*H/B*), ($\sigma_{ci}/\gamma B$), are of lesser importance with *RII* values of 70.4%, 50.11%, 17.54%, and 1.52%, respectively.

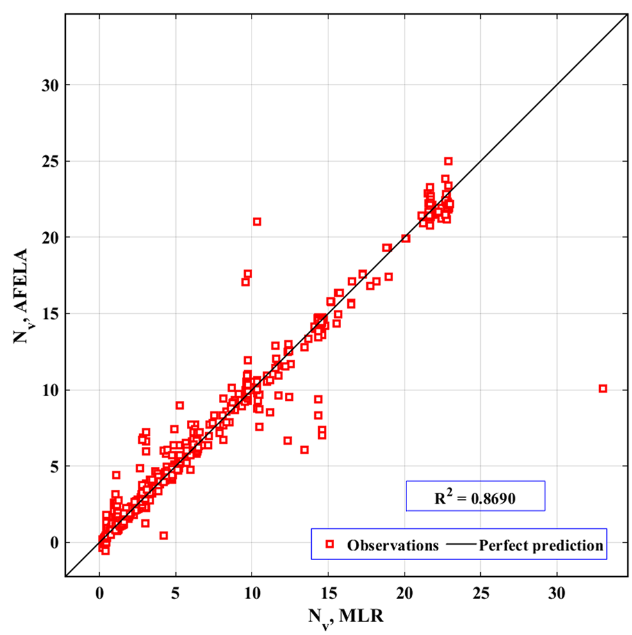

Fig. 15 Comparison of predicted value of N_v from *MLR* versus actual values of N_v obtained *AFELA* results

Artificial Neural Network (*ANN*)

Optimizing the number of hidden layers and neurons is crucial for improving the predictive power of an artificial neural network (*ANN*) model. This study demonstrates that an *ANN* model can accurately predict stability factor by utilizing a single hidden layer with varying numbers of neurons. The results presented in Fig. 17 show a clear relationship between the number of hidden neurons and the model's performance, indicating a significant improvement in performance when the number of neurons exceeds a certain threshold. It is expected that once this threshold is reached, the performance of the *ANN* model becomes stable.

Among the evaluated models, the "5-11-1" *ANN* model (consisting of 5 input variables, 11 hidden neurons, and 1 output) was found to be the most effective, displaying the lowest mean squared error (*MSE*), Root mean square value (*RMSE*) and the highest coefficient of determination (R^2) are as 1.1067, 1.051 and 0.992, respectively. Additionally, Fig. 18 demonstrates good agreement between the results obtained from the proposed *ANN* model and the finite element limit analysis (*FELA*) model.

Comparing the performance of the multiple linear regression (*MLR*) and *ANN* models, the latter demonstrated superior results, as indicated in Table 1. Therefore, the optimal *ANN* model with the "5-11-1" architecture can be utilized for predicting the stability factor from the *ANN* model.

The function can be used to generate output by considering weighted inputs and transfer function with an

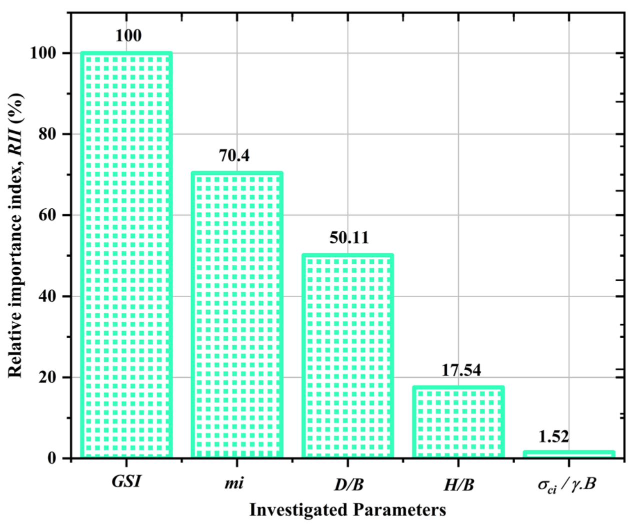

Fig. 16 Variation of relative importance index, (*RII*) on all dimensionless input variables

optimal *ANN* architecture. This network can simulate general functions and accurately predict functions with a finite number of discontinuities if the hidden layer has enough neurons. Weights for each parameter determine their impact on stability factor, and Eq. (12) represents the prediction equation using matrices from the ANN model.

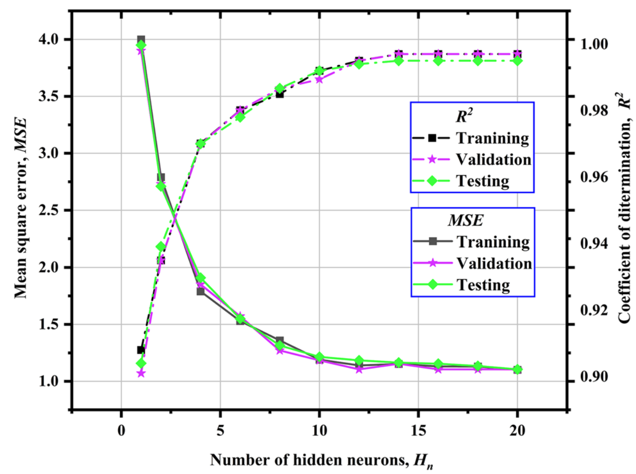

Fig. 17 Performance evaluation of square shaped tunnels versus the number of hidden neurons

$$Predictedvalue = \left[\sum_{i=1}^{N} IW2_i tansig\left(\sum_{j=1}^{J} IW1_{ij} x_j + b_{1i} \right) + b_2 \right] \tag{12}$$

The proposed *ANN* models represent *x* as input variables, *J* as the number of input variables, and *N* as the number of hidden neurons. Weight matrices *IW1* and *IW2* represent the hidden and output layers, while b_{1i} and b_2 represent the associated biases. The hidden weight matrix *IW1* is selected based on *N* and *J*, resulting in an output matrix with a single column. The input weight matrix *IW2* has the same number of rows as *N* and the same number of columns as the output neurons (*k*), with one column per neuron in the output layer.

Table 2 illustrates the utilization of weight and bias matrices, as constants within an optimized Artificial Neural Network (ANN) model, for the determination of the stability factor of strip footing over a horseshoe tunnel. The values obtained from the optimal ANN network can be leveraged to construct predictive equation functions, which can subsequently undergo rigorous testing on novel datasets, varying in data ranges, to enhance their accuracy and applicability.

Associated potential failure mechanism

This section describes the failure mechanisms of a strip footing under various scenarios where a tunnel is located at different distances and depths from the footing. The impact of governing parameters on the potential failure planes is also highlighted. The velocity field contours for the footing under different *H/B* ratios and depth ratios (*D/B* = 1, 2.5, and

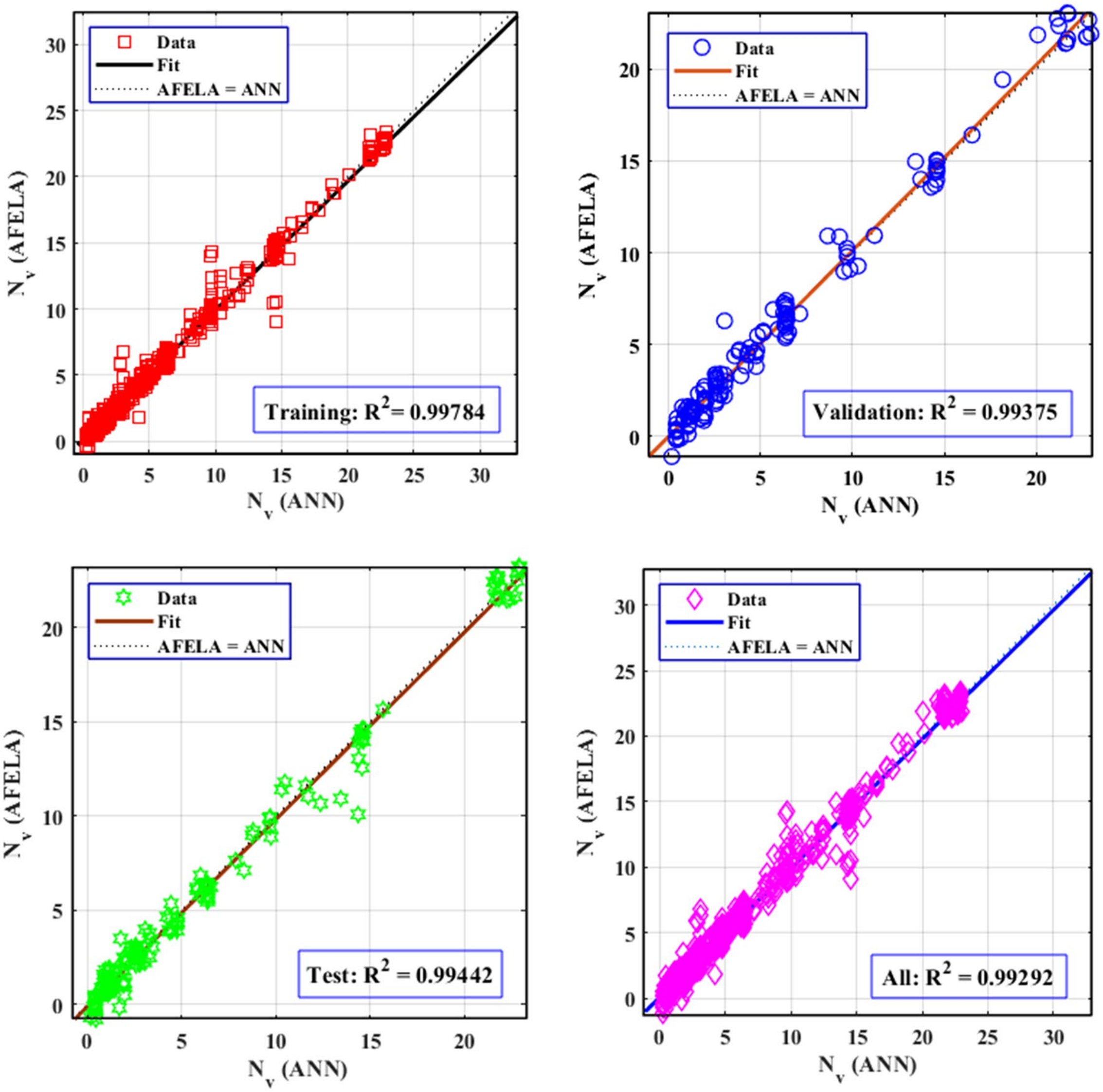

Fig. 18 Comparison of predicted value of N_γ from *ANN* versus N_γ obtained from *AFELA* results for the optimal *ANN* architecture (Model: 5-11-1) for horseshoe shaped tunnel

Table 1 Evaluation Metrics for Multiple Linear Regression (*MLR*) and Artificial Neural Networks (*ANN*) Performance

Machine learning approach	R^2	*RMSE*
Multiple linear regression (*MLR*)	0.869	3.127
Artificial Neural Network (*ANN*)	0.992	1.051

3) are shown in Figs. 19, 20 and 21 to illustrate the failure mechanisms.

In Fig. 19, for the case where $D/B=1$ and $H/B=0$, the tunnel experiences a combined failure of the roof and both sides of the vertical edge due to the high-stress concentration caused by the tunnel's placement directly below the footing at shallow depth. As the tunnel is situated away from the central vertical axis of the footing ($H/B=1$, 2, and 3), two failure planes originate from both corners of the footing, converging at the crest of the roof and the left bottom corner of the edge, affecting the entire periphery of the left edge. An additional failure plane extends from the crest of the tunnel's roof to the horizontal ground, resulting in the squeezing of the rock mass above this failure plane. For $H/B=4$ and 5, there is limited interaction between the tunnel edge and the footing, and an extra failure plane originates from the tunnel's roof, extending outwards until it intersects with the

Table 2 Neural network constants of the optimal model for stability prediction of strip footing laying over horseshoe tunnel

Hidden layer neurons (i)	Hidden layer bias (b_1)	Hidden weight, IW1					Output layer node, $k=1$	
		$\frac{\sigma_{ci}}{\gamma B}$ ($j=1$)	*GSI* ($j=2$)	*D/B* ($j=3$)	*H/B* ($j=4$)	m_i ($j=5$)	Output weight, IW2	Output bias, b_2
1	2.5835	−0.7442	0.7033	−0.0220	−1.7522	−0.2553	0.014	0.8727
2	−3.1188	1.4209	−2.8613	0.2099	−3.7487	2.9843	−0.6246	
3	1.6377	1.1937	−0.0849	−1.6579	3.6523	0.7118	0.2877	
4	−1.0048	−1.7435	−0.0252	−1.0875	1.1033	0.0995	0.3257	
5	−1.1481	0.6619	−1.7116	−0.0543	−0.2782	1.1423	0.2637	
6	0.4115	0.8294	0.0096	−0.8482	−3.9851	−0.0649	−0.4873	
7	−2.7780	−1.2147	2.1955	−1.3819	1.0203	0.1385	−0.7074	
8	−1.5262	−0.3698	0.8612	−2.5984	1.4403	−1.5077	0.0100	
9	−0.5110	−0.0839	0.2021	2.8771	0.1559	−1.5077	−0.1301	
10	0.8053	1.5020	−0.4906	−1.6203	1.2611	−0.1234	−0.0391	
11	0.3541	−0.6232	−0.0989	0.7402	−2.6560	−2.6611	0.2064	

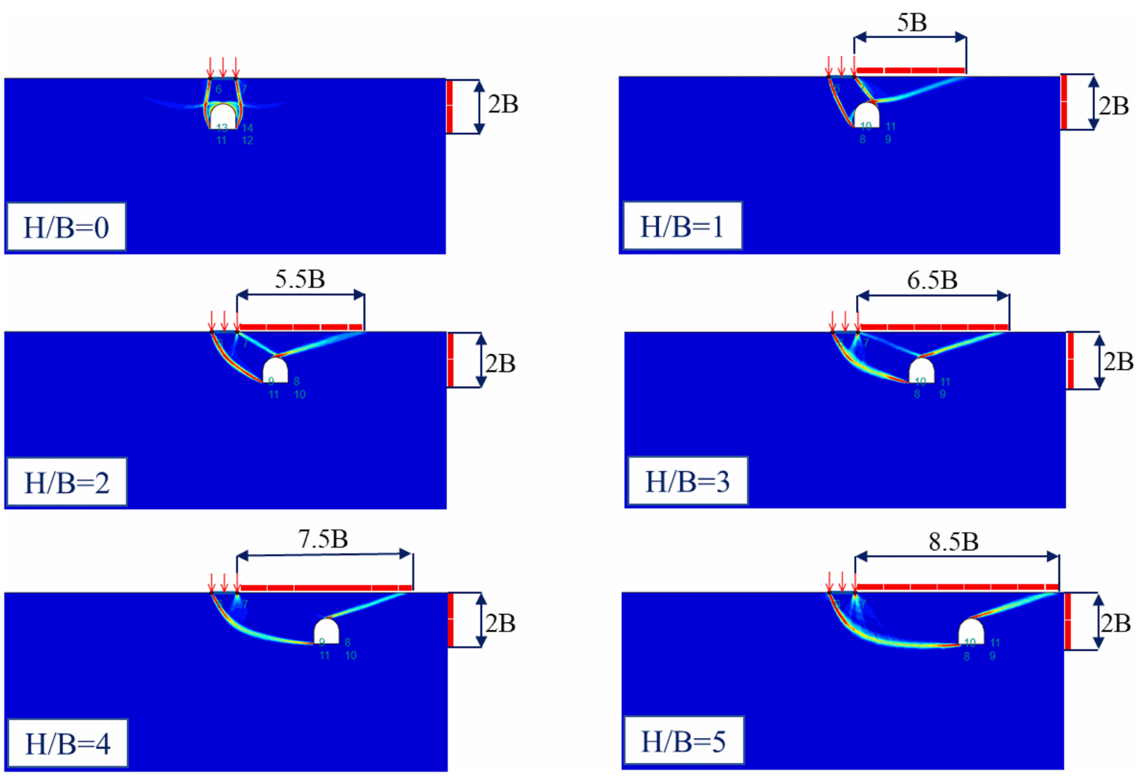

Fig. 19 Comparison of shear dissipation contours of footing above horseshoe shaped tunnel for various *H/B* with *D/B* = 1

horizontal ground surface. The zone of influence of the failure plane in the rock mass increases as the distance between the footing and tunnel increases horizontally. The maximum influence zone is 8.5*B* in the horizontal direction and 2*B* in the vertical direction from the central vertical axis of the footing and ground level, respectively for a given magnitude of *H/B* and *D/B*.

In Fig. 20, for the scenario where *D/B* = 2.5 and *H/B* = 0, 1, 2, and 3, the failure mode behaves similarly to the previous scenario. However, the maximum extent of the influence zone in the vertical direction enlarges to 3.5*B* due to the increased depth of the tunnel. For *H/B* = 4 and 5, the roof and left vertical edge of the tunnel interact with both corners of the footing through the failure plane, and the influence zone of the failure plane remains nearly constant at approximately 11*B*.

In Fig. 21, for the scenario where *D/B* = 3, the failure plane depicts a typical general shear failure below the

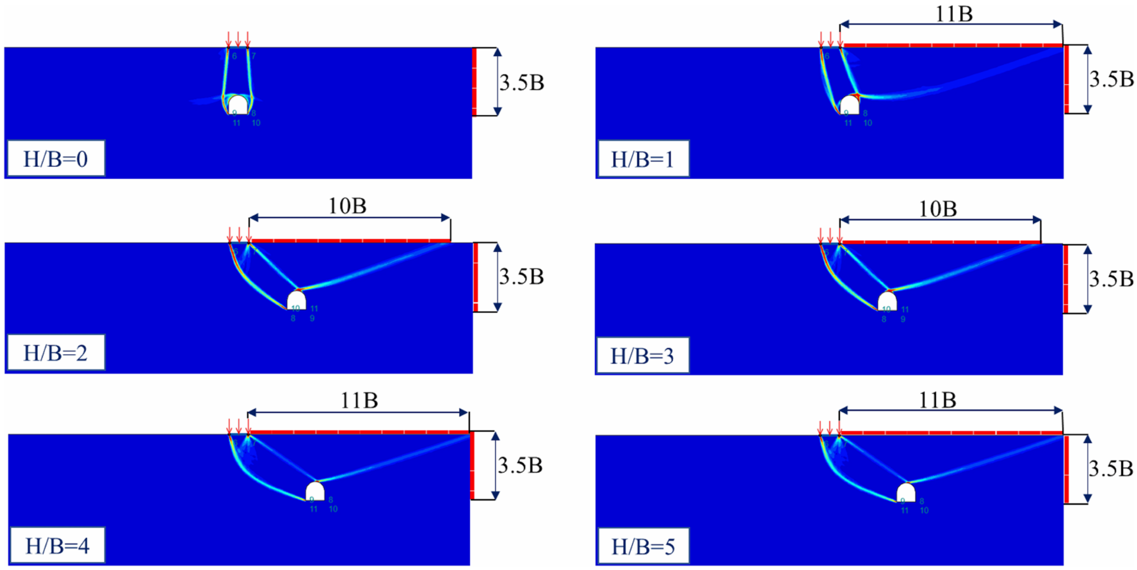

Fig. 20 Shear dissipation contours of footing above horseshoe shaped tunnel for various H/B with $D/B=2.5$

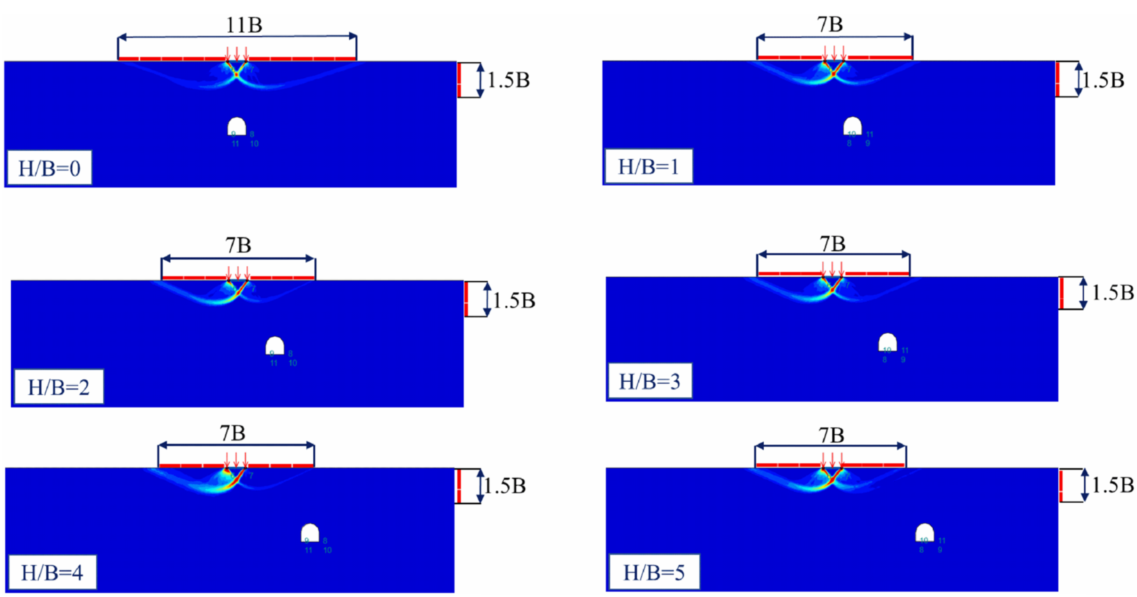

Fig. 21 Shear dissipation contours of footing above horseshoe shaped tunnel for various H/B with $D/B=3$

footing, similar to Terzaghi's failure mechanism for strip footing resting on semi-infinite soil mass (Craig 2004). The presence of the tunnel beyond the depth, $D/B \geq 3$, has no impact on the generated failure plane. The zone of influence within rock mass, which is affected by the failure plane, exhibits symmetry. Additionally, this zone extends to a distance of 3.5 times the width of footing on both sides for the given value of H/B (except $H/B=0$). This failure plane that has been observed in this study is similar to the one reported by Kumar and Chauhan (2022a), where a footing was situated above a circular unlined tunnel in a rock mass. The findings suggest that the presence of the tunnel beyond a depth ratio of $D/B \geq 3$ does not have any significant impact on the generated failure plane. As a result, the influence zone of the rock mass affected by the failure plane is symmetrical and extends up to a distance of $3.5B$ on both sides of the footing, for a given value of H/B (except when $H/B=0$).

Conclusions

In this study, the stability number (N_v) for a strip footing subjected to uniformly distributed loading above a horseshoe-shaped tunnel in rock mass was analysed using adaptive finite element limit analysis (*AFELA*) and dependability of N_v with of various positional and rock mass parameters, including the depth of the tunnel (*D/B*), the horizontal distance of the tunnel (*H/B*), the geological strength index (*GSI*), the normalized uniaxial compressive strength of the rock mass ($\sigma_{ci}/\gamma B$), and the material constant of the rock mass (m_i) was investigated. Generally, the magnitude of N_v increases with increasing *D/B* and *H/B*, but when $D/B \geq 3$, the magnitude of N_v remains constant for any given value of *H/B*, indicating that the presence of the tunnel has no impact on the stability of the footing. Increasing *GSI* and m_i tends to increase the magnitude of N_v, but the impact of $\sigma_{ci}/\gamma B$ on N_v is negligible. The failure mechanisms of tunnels can be classified into three categories based on the horizontal and vertical positions of the tunnels. These categories are as follows: (1) the combined failure of the roof and vertical edge of the tunnel, (2) vertical edge failure only, and (3) general shear failure below the footing, which is similar to the one described in Terzaghi's failure mechanism for strip footings resting on semi-infinite soil mass. In the third category, there is no interaction between the tunnel and the footing is observed. A stable and high-performing neural network model with a single hidden layer of fifteen neurons was constructed and validated for evaluating the stability factor of the strip footing. These models and equation are specifically customized for the ranges outlined in the present study and can be employed for assessing new data with great assurance. The combination of *AFELA* with artificial neural network (*ANN*) and multiple linear regression (*MLR*) models is proposed as a reliable tool for geotechnical engineers to assess the stability of strip footing in inference of tunnel. The *ANN* and *MLR* models offer faster prediction of tunnel stability compared to *AFELA*.

Acknowledgements The authors of this article gratefully acknowledge the anonymous reviewers and Editor for their constructive critical comments which has helped the authors to improve the manuscript substantially. The authors express their gratitude for the computing facility made available by the Department of Civil Engineering, MMMUT, Gorakhpur, India.

Author contributions Conceptualization: AK, VBC, and PK; writing original draft and editing: AK, and PK; validation: AK, and PK; data curation and analysis: AK, and PK; methodology: AK, and VBC; project supervision: VBC; review and editing: VBC.

Funding This research did not receive any specific grant from funding agencies in the public, commercial, or not-for profit sectors.

Data availability All the data associated with the study are present in the manuscript itself.

Declarations

Conflict of interest On behalf of all authors, the corresponding author states that there is no conflict of interest.

References

Ansari A, Rao KS, Jain AK (2023) Ansari A (2023) Deep learning model for predicting tunnel damages and track serviceability under seismic environment. Model Earth Syst Environ 9:1349–1368. https://doi.org/10.1007/s40808-022-01556-7

Atici U (2011) Prediction of the strength of mineral admixture concrete using multivariable regression analysis and an artificial neural network. Expert Syst Appl 38:9609–9618

Azarafza M, Asghari-Kaljahi E, Ghazifard A, Akgun H (2021) Application of fuzzy expert decision-making system for rock slope block-toppling modeling and assessment: a case study. Model Earth Syst Environ 7:159–168. https://doi.org/10.1007/s40808-020-00877-9

Badie A, Wang MC (1984) Stability of spread footing above void in clay. J Geotech Eng 110(11):1591–1605. https://doi.org/10.1061/(ASCE)0733-9410(1984)110:11(1591)

Bilim C, Atis CD, Tanyildizi H (2008) Karahan O (2008) Predicting the compressive strength of ground granulated blast furnace slag concrete using artificial neural network. Adv Eng Softw 40:334–340

Carranza-Torres CM (1998) Self-similarity analysis of the elastoplastic response of underground openings in rock and effects of practical variables. University of Minnesota, Minneapolis

Chauhan VB, Kumar P, Keawsawasvong S (2022) Limit analysis solution for ultimate bearing capacity of footing resting on the rock mass with a circular void subjected to line loading. Indian Geotech J. https://doi.org/10.1007/s40098-022-00676-2

Chayut N, Suraparb K, Thira J, Lowell C, Meghdad P, Kongtawan S, Rungkhun B, Chanachai T (2022) Data-driven prediction of stability of rock tunnel heading: an application of machine learning models. Infrastructures 7:148. https://doi.org/10.3390/infrastructures7110148

Fam MA, Cascante G, Dassault MB (2002) Large small strain properties of sand subjected to local voids increases. J Geotech Environ Eng 128(12):1018–1025. https://doi.org/10.1061/(ASCE)1090-0241(2002)128:12(1018)

Fraldi M, Guarracino F (2010) Analytical solutions for collapse mechanisms in tunnels with arbitrary cross-sections. Int J Solids Struct 47(2):216–223. https://doi.org/10.1016/j.ijsolstr.2009.09.028

Hoek E, Brown ET (1980) Empirical strength criterion for rock masses. J Geotech Eng Div 106(9):1013–1035. https://doi.org/10.1061/AJGEB6.0001029

Hoek E, Carranza-Torres C, Corkum B (2002) Hoek-Brown failure criterion—2002 edition. Proc N Am Rock Mech Soc Meet Tor Can 1(1):267–273

Jaiswal S, Chauhan VB (2021) Ultimate bearing capacity of strip footing resting on rock mass using adaptive finite element method. J King Saud Univ-Eng Sci. https://doi.org/10.1016/j.jksues.2021.09.004

Jearsiripongkul T, Keawsawasvong S, Banyong R, Seehavong S, Sangjinda K, Thongchom C et al (2022) Stability evaluations of unlined horseshoe tunnels based on extreme learning neural

network. Computation 10:81. https://doi.org/10.3390/computation10060081
Jearsiripongkul T, Keawsawasvong S, Thongchom C, Ngamkhanong C (2022a) Prediction of the stability of various tunnel shapes based on Hoek-Brown failure criterion using artificial neural network (ANN). Sustainability 14:4533. https://doi.org/10.3390/su14084533
Jintara L, Shiau J, Keawsawasvong S, Seehavong S, Jamsawang P (2022) Design equations for predicting stability of unlined horseshoe tunnels in rock masses. Buildings 12:1800. https://doi.org/10.3390/buildings12111800
Jun L, Zhang Q, An L, Guanghui C (2022) Stability analysis of the horseshoe tunnel face in rock masses. Materials 15:4306. https://doi.org/10.3390/ma15124306
Keawsawasvong S, Shiau J, Limpanawannakul K, Panomchaivath S (2022) Stability charts for closely spaced strip footings on Hoek-Brown rock mass. Geotech Geol Eng 40:3051–3066. https://doi.org/10.1007/s10706-022-02077-x
Kiyosumi M, Kusakabe O, Ohuchi M (2011) Model tests and analyses of bearing capacity of strip footing on stiff ground with voids. J Geotech Geoenviron Eng 137(4):363–375. https://doi.org/10.1061/(ASCE)GT.1943-5606.0000440
Kumar P, Chauhan VB (2022a) On the eccentrically loaded strip footing resting over a circular cavity in the rock mass: adaptive finite-element analysis, observations, and recommendations. Int J Geomech 23(2):04022287. https://doi.org/10.1061/IJGNAI.GMENG-7985
Kumar P, Chauhan VB (2022b) Bearing capacity of strip footing resting above a circular void in the rock mass using adaptive finite element method. Innov Infrastruct Solut 7:72. https://doi.org/10.1007/s41062-021-00666-y
Kumar P, Chauhan VB (2022c) Ultimate bearing capacity of a foundation on the rock media due to the presence of a circular void: design tables, failure mechanism, and recommendations. Arab J Geosci 15(15):1–11. https://doi.org/10.1007/s12517-022-10620-6
Lai VQ, Sangjinda K, Keawsawasvong S, Eskandarinejad A, Chauhan VB, Sae-Long W, Limkatanyu S (2022a) A machine learning regression approach for predicting the bearing capacity of a strip footing on rock mass under inclined and eccentric load. Front Built Environ. 8:962331. https://doi.org/10.3389/fbuil.2022.962331
Lai VQ, Shiau J, Promwichai T, Limkatanya S, Banyong R, Keawsawasvong S (2022b) Modelling soil stability in wide tunnels using FELA and multivariate adaptive regression splines analysis. Model Earth Syst Environ. https://doi.org/10.1007/s40808-022-01595-0
Lai VQ, Lai F, Yang D, Shiau J, Yodsomjai W, Keawsawasvong S (2022c) Determining seismic bearing capacity of footings embedded in cohesive soil slopes using multivariate adaptive regression splines. Int J Geosynthet Ground Eng 8(4):46. https://doi.org/10.1007/s40891-022-00390-2
Lai VQ, Shiau J, Van CN, Tran HD, Keawsawasvong S (2022d) Bearing capacity of conical footing on anisotropic and heterogeneous clays using FEA and ANN. Marine Georesour Geotechnol. https://doi.org/10.1080/1064119X.2022.2113485
Lai VQ, Shiau J, Promwichai T, Limkatanyu S, Banyong R, Keawsawasvong S (2022e) A machine learning regression approach for predicting the bearing capacity of a strip footing on rock mass under inclined and eccentric load. Front Built Environ 8:152. https://doi.org/10.3389/fbuil.2022.962331
Lee JK, Jeong S, Ko J (2014) Undrained stability of surface strip footings above voids. Comput Geotech 62:128–135. https://doi.org/10.1016/j.compgeo.2014.07.009
Obaidur R, Jyant K (2020) Stability analysis of twin horse-shoe shaped tunnels in rock mass. Tunnel Underground Sp Technol. 98:103354. https://doi.org/10.1016/j.tust.2020.103354
Optum G2 (2020) Finite element program for geotechnical analysis, Optum Computational Engineering. www.optum.com. Accessed 04 Apr 2023
Park YS, Lek S (2016) Chapter 7—artificial neural networks: multilayer perceptron for ecological modeling. In: Jørgensen SE (ed) Developments in environmental modelling. Elsevier, Amsterdam
Sayan S, Suraparb K, Chayut N, Sorawit S, Kongtawan S, Thira J, Chanachai T, Peem N (2022) Neural network-based prediction model for the stability of unlined elliptical tunnels in cohesive-frictional soils. Buildings 12:444. https://doi.org/10.3390/buildings12040444
Soleiman DM, Lazemi HA, SaeedModaghegh HR (2019) Estimation of the drop modulus using the brittleness index of intact rock and geological strength index of rock mass, case studies: Nosoud and Zagros tunnels in Iran. Model Earth Syst Environ 5:479–492. https://doi.org/10.1007/s40808-019-00577-z
Ukritchon B, Keawsawasvong S (2018) Lower bound limit analysis of an anisotropic undrained strength criterion using second-order cone programming. Int J Numer Anal Methods Geomech 42(8):1016–1033. https://doi.org/10.1002/nag.2781
Waltham T, Waltham AC, Bel FG, Culshaw MG (2005) Sinkholes and subsidence; karst and cavernous rock in engineering and construction. Springer Science and Business Media, New York
Wang MC, Badie A (1985) Effect of underground void on foundation stability. J Geotech Eng 111(8):1008–1019. https://doi.org/10.1061/(ASCE)0733-9410(1985)111:8(1008)
Wu G, Zhao M, Zhang R, Liang G (2020a) Ultimate bearing capacity of eccentrically loaded strip footings above voids in rock masses. Comput Geotech 128:103819. https://doi.org/10.1016/j.compgeo.2020.103819
Wu Z, Wong LNY (2015) Modeling the progressive failure in rock slopes based on the fracture mechanics approach using the numerical manifold method. In: Proceedings of 13th ISRM international congress of rock mechanics innovations in applied and theoretical rock mechanics. International Society for Rock Mechanics, Lisbon
Xiao Y, Zhao M, Zhao H (2018) Undrained stability of strip footing above voids in two-layered clays by finite element limit analysis. Comput Geotech 97:124–133. https://doi.org/10.1016/j.compgeo.2018.01.005
Xiao Y, Zhao M, Zhang R, Zhao H, Wu G (2019) Stability of dual square tunnels in rock masses subjected to surcharge loading. Tunnel Underground Sp Technol. 92:103037. https://doi.org/10.1016/j.tust.2019.103037
Yodsomjai W, Lai VQ, Banyong R, Chauhan VB, Thongchom C, Keawsawasvong S (2022) A machine learning regression approach for predicting basal heave stability of braced excavation in non-homogeneous clay. Arab J Geosci 15(9):873. https://doi.org/10.1007/s12517-022-10161-y
Zhang J, Feng T, Yang J, Yang F, Gao Y (2018) Upper-bound stability analysis of dual unlined horseshoe-shaped tunnels subjected to gravity. Comput Geotech 97:103–110
Zhao L, Huang S, Zeng Z, Zhang R, Tang G, Zuo S (2021) Study on the ultimate bearing capacity of a strip footing influenced by an irregular underlying cavity in karst areas. Soils Found 61(2):259–270. https://doi.org/10.1016/j.sandf.2020.09.011